ACS OMEGA

Open Access

http://pubs.acs.org/journal/acsodf

Article

MXene Clay (Ti2C)-Containing In Situ Polymerized Hollow Core−Shell Binder for Silicon-Based Anodes in Lithium-Ion Batteries

Mi Tian, Wenjun Gan,* and Eun-Suok Oh*

Cite This: *ACS Omega* 2023, 8, 49302−49310

Read Online

ACCESS | Metrics & More | Article Recommendations | Supporting Information

ABSTRACT: Silicon, an attractive anode material, suffers fast capacity fading due to the electrical isolation from massive volumetric expansion upon cycling. However, it holds a high theoretical capacity and low operation voltage in its practical application. In this study, a new water-based binder, MXene clay/hollow core−shell acrylate composite, was synthesized through an in situ emulsion polymerization technique to alleviate the fast capacity fading of the silicon anode efficiently. The efficient introduction of conductive MXene clay and the hollow core−shell structure, favorable to electron and ion transport in silicon-based electrodes, gives a novel conceptual design of the binder material. Such a strategy could alleviate electrical isolation after cycling and promises better electrochemical performance of the high-capacity anodes. The effect of the MXene introduction and hollow core−shell on the binder performance is thoroughly investigated using various characterization tools by comparison with no MXene-containing, core−shell acrylate, and commercial styrene−butadiene latex binders. Consequently, the silicon-based electrode containing the MXene clay/hollow core−shell acrylate binder exhibits a high capacity retention of 1351 mAh g^{-1} at 0.5C after 100 cycles and good rate capability of over 1100 mAh g^{-1} at 5C.

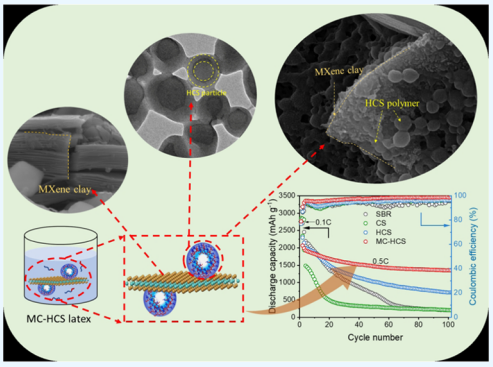

1. INTRODUCTION

Silicon (Si) as an anode material has attracted significant attention due to its advantages of high theoretical capacity (~4200 mAh/g), low operation potential (<0.5 V vs Li/Li^+), and abundant resources.[1] However, Si anodes suffer from severe capacity fading during the lithiation/delithiation process, resulting from Si's massive volumetric expansion (~300%). The repetitive volumetric change of Si worsens the particle-to-particle contacts, leading to the electrical and ionic isolation of Si electrodes and the delamination of the electrode from the current collector.[2] Furthermore, the enormous volumetric expansion results in cracks in the solid electrolyte interphase (SEI) and causes additional SEI layer growth on the surface of Si.[3] These undesirable phenomena have hindered their application in the energy storage field. In order to alleviate the irreversible expansion and shrinkage of silicon, tremendous research studies have been conducted on silicon structure design,[4−6] electrolyte modification,[7−9] and multifunctional binders.[10−12] The binder gives an alternative option that can effectively suppress the problems due to its facile fabrication process and low cost.

The fundamental role of a binder in an electrode is to maintain the conductive network of the electrode through the cohesion of the electrode components (e.g., active material and conductive agent) and their adhesion to the current collector during cell operation.[13] Thus, the binder plays a significant role in the mechanical stability of electrodes and their long-term cycling performance. Organic-based poly(vinylidene fluoride) (PVdF) has been commercially used in LIBs. However, silicon interacts with the surface by weak van der Waals forces, leading to a poor cycling performance and rate capability. Additionally, PVdF is dissolved only in a toxic organic solvent (e.g.,*N*-methyl-2-pyrrolidone, NMP), which causes environmental concerns during slurry preparation. Although commercial styrene−butadiene latex (SBL) is a water-dispersed binder, its use is limited due to its worse effect of suppressing silicon expansion and maintaining electrical paths when used in silicon-based electrodes. Above all, apart from better adhesion and environmental friendliness, the binders in silicon-based anodes are expected to have better functions to address considerable expansion and electrical isolation. Various efforts are emerging, such as self-healing polymeric binders to alleviate expansion and repair electrical network, grafted binders containing electrical and ionic conduction segments to improve conductivity, and multifunctional binders to enhance the comprehensive capability.[12,14−16]

Two-dimensional (2D) materials have recently been widely used in energy storage due to their electronic conduction and

Received: October 6, 2023
Revised: November 29, 2023
Accepted: November 30, 2023
Published: December 13, 2023

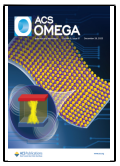

good mechanical properties. MXene, as a novel 2D nanomaterial, has attracted significant attention and has been applied in a variety of industries, such as catalysis,[17,18] wearable sensors,[19,20] and energy storage,[21,22] since it was first discovered in 2011.[23] Compared with 2D graphene materials, the MXene is more hydrophilic and holds wealthy functional groups (e.g., −O, −F, and −OH) on its surface.[24] These outstanding properties make the MXene implementable in water and allow some reactions and interactions with other functional groups (e.g., −OH, −COOH, or −CN).[25] Many researchers reported MXene/polymer composites such as MXene with poly(ethylene oxide) (PEO),[26] poly(vinyl alcohol) (PVA),[27,28] polyacrylamide (PAAm),[20] etc. The MXene interacts with polymers by hydrogen bonding force, van der Waals attraction, and electrostatic interaction.[29−31] Combining MXene with polymers can enhance the properties and performances of the composites, including mechanical properties, solution stability, and especially electrical conductivity.[32]

Inspired by the conception, we introduce a conductive MXene to water-based polymerization and obtain a water-based MXene/polymer composite binder to compensate for the shortage of the water-based binder without electrical conductivity. Primarily, a water-based binder with a unique hollow core−shell structure was synthesized on the surface of the MXene by in situ emulsion polymerization. Removing core polymeric components from core−shell-structured polymers achieved a hollow core−shell structure. Its empty inside allows Li ions to shuttle during the charge/discharge process. The removed cores also help the electrode slurry to maintain high viscosity in the electrode coating process.

On the other hand, the outer shell design has essential binder properties such as adhesion and mechanical strength, composed of poly(acrylonitrile-butyl acrylate-styrene). The −CN groups in acrylonitrile (AN) provide good adhesion in electrodes, the styrene (St) is typically used to improve mechanical strength,[33] and the butyl acrylate (BA) imparts a flexible behavior for the binder to tolerate the deformation during cell operation.[34] The commercial water-dispersed SBL binder was used as a reference binder. The structure of the MXene clay/hollow core−shell composite binder (abbreviated as MC-HCS) was confirmed by TEM and SEM spectroscopies, and its physical and electrochemical characterization is examined through various methods.

2. MATERIALS AND METHODS

2.1. Materials. Methyl methacrylate (MMA), methacrylic acid (MAA), and butyl acrylate were purchased from Sigma-Aldrich. Styrene and acrylonitrile were obtained from Samchun pure Chemical Co., Ltd. (South Korea) and Junsei Chemical Co., Ltd. (Japan), respectively. Sodium hydroxide powder (NaOH) was purchased from the OCI Company Ltd. Ammonium persulfate powder (APS) and sodium dodecylbenzenesulfonate powder (SDBS) were purchased from Sigma-Aldrich. All powder products were dissolved into distilled water. The MXene clays (MCs) were obtained from Suzhou BKnano Material Co. Ltd. (Suzhou, China) and sonicated before use.

2.2. Synthesis of Core−Shell, Hollow Core−Shell, and MXene Clay/Hollow Core−Shell Binders. The polymerization is conducted in a four-neck round-bottom reactor with a vigorous stirrer, reflux condenser, nitrogen gas inlet system, and feeding devices. The recipes for synthesizing core−shell, hollow core−shell, and MXene/hollow core−shell binders are listed in Table S1 in the Supporting Information with the reaction conditions. Seed latex was first polymerized to control the particle sizes. Multistep emulsion polymerization sequentially synthesized core and shell polymers in the seed latex. The whole polymerization for CS latex proceeded for 5 h to core polymers and another 4 h to shell polymers with 200 rpm stirring at 80 °C under a nitrogen atmosphere. Noteworthily, the core-to-shell mass ratio was fixed at 1−4 to obtain relatively homogenous latex with a regular round shape. The HCS binder is completed through the alkalization treatment of the CS latex. The alkalization process is conducted to remove the inner core polymers and to form a hollow core−shell structure. The MC-HCS binder synthesis uses the same procedure as that for the HCS latex. This water-dispersed MCs solution was used in the seeding process instead of pure water. The MCs were first dispersed in distilled water by sonication for 2 h under a nitrogen atmosphere, and then, seed monomers were added for subsequent in situ polymerization on MCs. The exact amount of MCs used at the core polymerization step is given. Figure S1 shows the photographs of the sonicated MC solution and MC-HCS latex binder, where the binder latex contains 1.67 wt % of MC.

2.3. Preparation of Binder Films, Electrodes, and Cells. The mixture of binder solution was composed of 80 wt % binders and 20 wt % of thickener carboxymethyl cellulose (CMC, Daicel FineChem Ltd., Japan) and dried overnight in a convection oven at 40 °C on a Teflon substrate to obtain a composite binder film. The thickness of the binder films ranged from 450 to 600 μm. A completely dry binder film is sandwiched in a stainless-steel cell (SS/binder film/SS).

The slurry is prepared with a silicon (Si, 50−60 nm, KCC Co. Ltd.) active material, Super P (SP, PHOENIX) conductive agent, binders, and the thickener CMC. The mass ratio in the slurry was 60:20:10:10 for Si/SP/CMC/binder. After mixing well in a planetary ball mill (Pulverisette 7, Fritsch), the slurry was coated on copper foil with the doctor blade method and dried in a convection oven for 30 min at 60 °C. The mass loading of Si electrodes was 0.7−1 mg cm^{-2}. Before the assembly, the electrodes were dried in a vacuum oven at 70 °C overnight and fabricated into CR2032-type coin cells in an argon-filled glovebox. Here, a lithium chip (MTI Korea Co. Ltd.) and 1.15 M $LiPF_6$ ethylene carbonate/fluoroethylene carbonate/propylene carbonate/diethyl carbonate/ethyl methyl carbonate (EC/FEC/PC/DEC/EMC = 20:10:5:40:25 in volume) (Soulbrain Co., Ltd., Korea) were used as the counter electrode and electrolyte, respectively. A polypropylene separator (Celgard LLC) was placed between the working Si and counter Li electrodes.

2.4. Physical and Electrochemical Characterization of the Binder Solution, Binder Film, Electrode Sheets, and Half-Cells. First, Fourier transform infrared (FT-IR) spectroscopy of polymeric binders is performed through a Nicolet iS5 Thermo Fisher Scientific. Raman spectroscopy is performed using a DXR Raman microscope (Thermo Fisher Scientific) under 532 nm laser excitation. Differential scanning calorimetry (DSC, Q50 of TA Instruments) was used to measure the glass transition temperature at a heating/cooling rate of 10 °C/min under a nitrogen atmosphere. Using the same apparatus, the thermal stability was investigated with a 20 °C/min ramp under a nitrogen flow. The viscosity tests were performed through a rheometer (HR20, TA-Instruments) under a shear rate in the range of 0.1−1000/s. Scanning electron microscopy (FE-SEM, JSM-600F, JEOL, Japan) and transmission electron microscopy (FE-TEM) were used to investigate the morphologies of binders. The wettability and swelling ability are examined

https://doi.org/10.1021/acsomega.3c07752
ACS Omega 2023, 8, 49302−49310

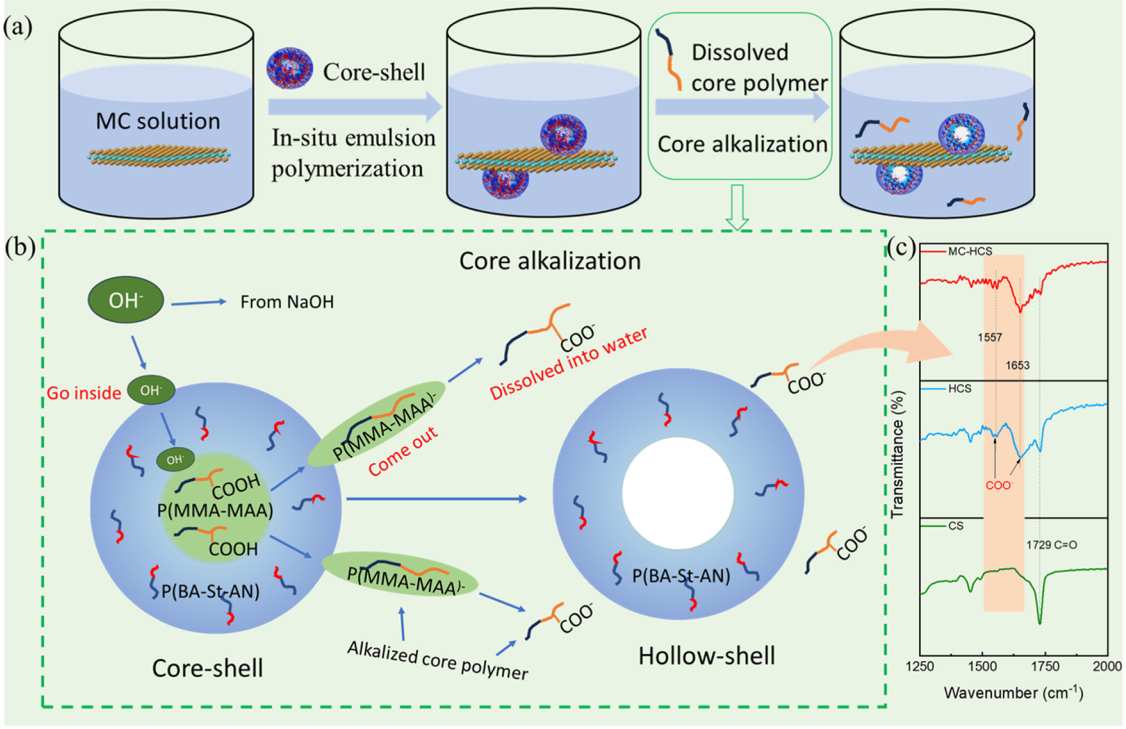

Figure 1. Synthesis process of the in situ polymerized MC-HCS binder: (a) schematic synthesis and (b) alkalization process and (c) FT-IR spectra.

through the contact angle (Biolin Scientific, Theta Life) and electrolyte uptake. The contact angle measurement is conducted at room temperature by dropping the electrolyte solution on the binder film and recording the angle change for 1 min. The binder films soak in the electrolyte for 4 h to obtain the uptake ratio calculated through eq 1

$$\text{electrolyte uptake } (\%) = \frac{w_1 - w_0}{w_0} \times 100\% \quad (1)$$

Here, w_0 and w_1 are the weights of the binder films before and after absorption of the electrolyte, respectively.

To calculate the ionic conductivity, electrochemical impedance spectroscopy (EIS, VSP, BioLogic Science Instruments) was implemented at OCV in the frequency range from 10 Hz to 100 kHz using a stainless-steel cell and eq 2

$$\delta_i = \frac{l}{R \times A} \quad (2)$$

where δ is the ionic conductivity, l is the thickness of the binder film, R is the bulk resistance obtained from EIS, and A is the area of the binder film. The electronic conductivities of HCS and MC-HCS were measured using the Wagner−Hebb method.

The electrode sheet's adhesion strength was measured through a 180° peel force of 2 cm wide strips with a texture analyzer (TA-Plus, Lloyd Instruments Ltd.) at a propagation speed of 60 mm min^{-1}. The resistance and resistivity of the electrode sheet were investigated using a 46-multipoint probe system (RM2610, Hioki Corp., Japan) at room temperature.

Long cycling performance of silicon electrodes in a coin cell was examined using the charge/discharge process at 0.1C for the first 2 cycles and 0.5C for the following 100 cycles. Cells were operated at various current densities for rate efficiency testing from 0.1C to 5C. Both experiments were operated in PNE solution (PEB0501 system, Korea) in a voltage window of 0.005−1.5 V. Cyclic voltammetry (CV) and EIS of the cells are performed using a potentiostat (VSP, BioLogic Science Instruments). CV scans were carried out with a scanning rate of 0.5 mV s^{-1} in the voltage range of 0.0−1.5 V. The EIS was recorded in a frequency range of 0.01 Hz−100 kHz at 0.2 V vs Li/Li^+ and with an amplitude voltage of 7 mV.

3. RESULTS AND DISCUSSION

Figure 1(a) shows a schematic synthesis of the MC-HCS binder. We first synthesized a core−shell structure on the MXene surface by in situ polymerization. Later, inner core polymers were dissolved through alkalization treatment to obtain a hollow core−shell structure. During the alkalization process as shown in Figure 1(b), the hydroxyl anion (OH^-) from sodium hydroxide is easier to penetrate through the outer shell when the temperature is over the glass transition temperature (T_g) and then reacts with a carboxyl group (COOH) in the core polymer.[35] After the alkalization treatment, the core polymers come out of the core−shell structure and finally dissolve in aqueous medium. Because the T_g of the CS (measured by DSC in Figure S2) was 13.8 °C, the alkalization occurred at 70 °C, which is significantly higher than the T_g of the CS polymer and it is easier for OH^- to be transported inside of the shell.

FTIR and Raman spectroscopy were performed to confirm the successful in situ polymerization and are shown in Figures 1c and S3. The peak observed at 1452 cm^{-1} is associated with the phenyl C_6H_6 stretching vibration of St,[33] and there is also a weak vibration peak at 2276 cm^{-1} contributing to the CN group.[36] The vibration at 1162 cm^{-1} has been attributed to the C−O in R−COO−R of MMA and BA. The intensively strong peak at 1729 cm^{-1} belongs to C═O of BA and MMA, and in the case of CS latex, it also belongs to COOH in MAA of the core polymer.[37] The peak related to COO^- in the dissolved core polymer $P(MMA\text{-}BA\text{-}MAA)^-$ can be observed at 1557 cm^{-1}.[38] On the other hand, the COO^- vibration influences the presence of the two C═O peaks at 1653 and 1729 cm^{-1}. The COO^-

https://doi.org/10.1021/acsomega.3c07752
ACS Omega 2023, 8, 49302−49310

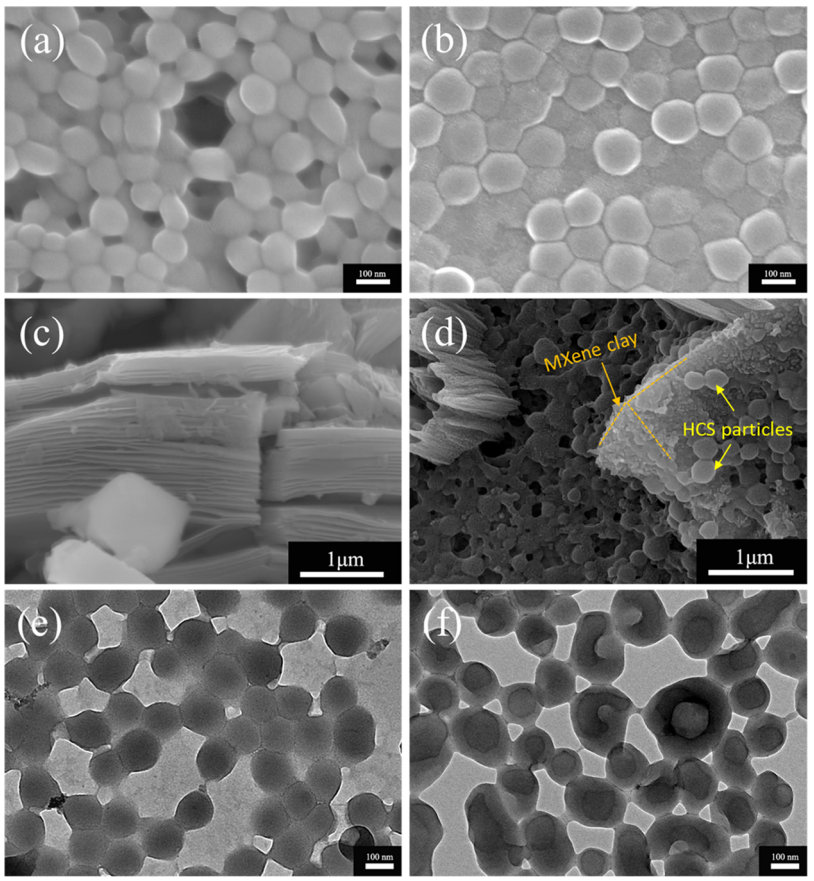

Figure 2. FE-SEM images of (a) CS particles, (b) HCS particles, (c) MC, and (d) MC-HCS binder. FE-TEM images of (e) CS and (f) HCS particles.

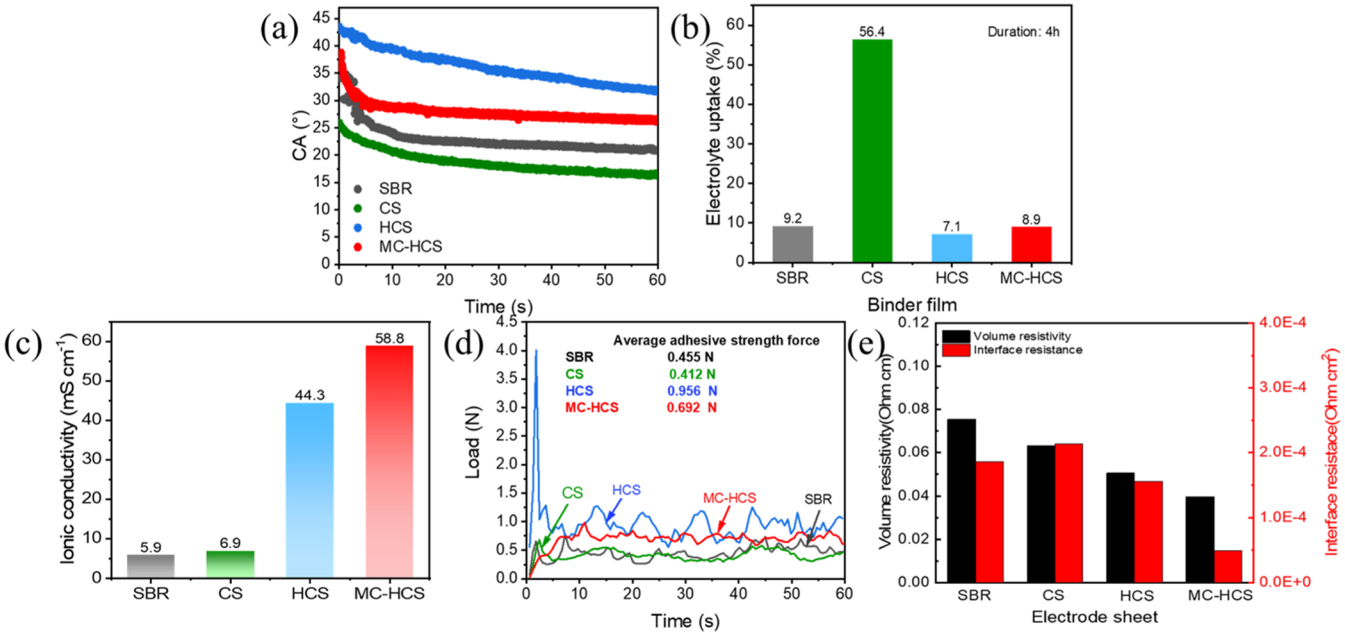

Figure 3. (a) Electrolyte contact angle change in 60 s, (b) electrolyte uptake for 4 h, (c) ionic conductivity, (d) adhesion strength, and (e) electrical resistance of the silicon electrodes composed of different binders.

groups exist only in the HCS and MC-HCS binder. The shift of −COOH to COO^- implies that the inner core polymer was successfully alkalized. The Raman shift in Figure S3b shows that the vibrations of Ti−O, C−Ti, and C−F of MCs are observed only in the MC-HCS binder. Moreover, the viscosity of HCS and MC-HCS latex shown in Figure S4 is more significant than that of the CS binder latex, proving that the core polymers have dissolved into water after alkalization, increasing viscosity. SEM and TEM further investigated the morphologies of CS, HCS, and MC-HCS.

https://doi.org/10.1021/acsomega.3c07752
ACS Omega 2023, 8, 49302−49310

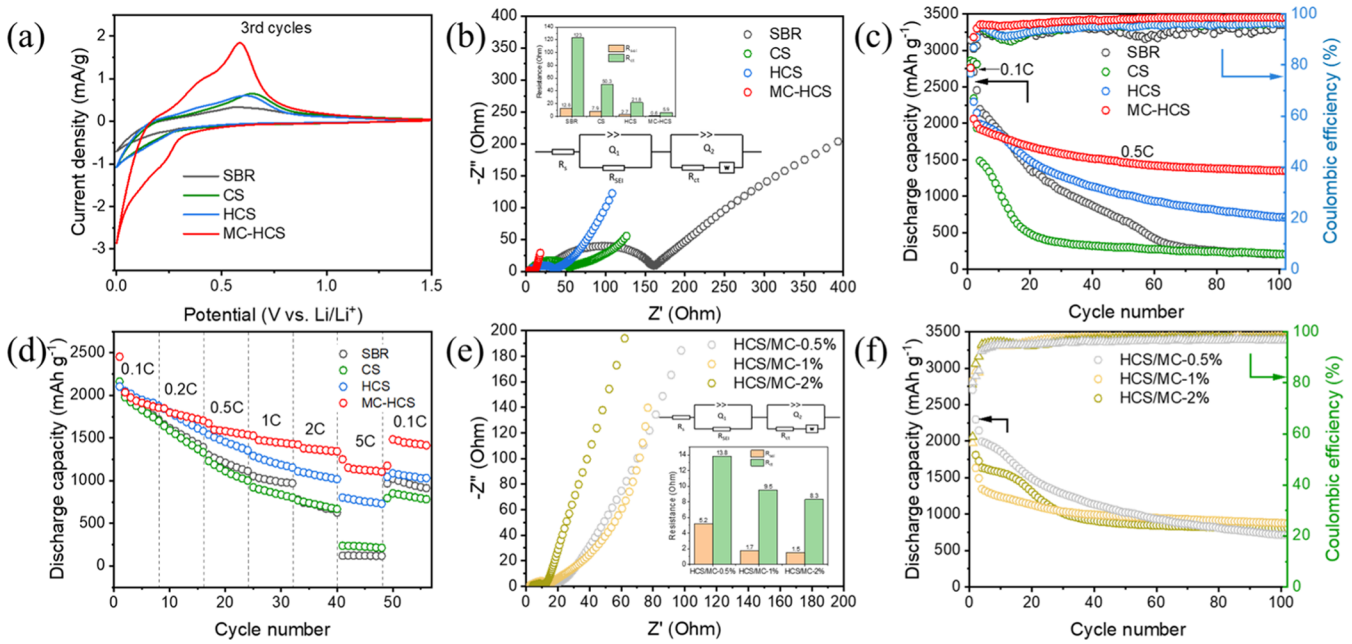

Figure 4. Electrochemical performances of the Si electrodes composed of different binders: (a) CV profiles of the third cycles, (b) EIS spectra of the 100-cycled Si-based electrodes, (c) cycling performance, and (d) rate capability. The EIS spectra and cycling performance of the Si electrodes fabricated with different amounts of physically mixed MCs (e, f), respectively.

FE-SEM images shown in Figure 2a–d indicate that the particles of the CS and HCS binder have a spherical structure, and MCs have a multistorey structure. Figure 2d shows polymer particles in situ polymerized on the surfaces of the MCs. More definite morphologies of the CS and HCS are observed using FE-TEM. Figure 2e demonstrates the structure of the CS binder in that light outer shells wrap the dark inner core part. In Figure 2f, however, the inner cores of the HCS are lighter when compared to those of the CS particle. This explains why the empty-core structure of the HCS forms successfully with the alkalization process.

The wettability and swelling of the binder film in the organic electrolyte were examined through the contact angle (CA) and electrolyte uptake. The results are shown in Figure 3a,b, respectively. Consistently, the hollow core–shell samples, HCS and MC-HCS, show a lower electrolyte uptake below 9% (7.1 and 8.9%, respectively) in 4 h, which is close to that of the conventional SBR binder and is much smaller than that of the core–shell CS binder of 56.4%. The CS binder film suffers such a high electrolyte uptake because the hydrophobic segments in the core polymer of the binder quickly absorb the organic electrolyte solution.[39] As already known, relatively high electrolyte uptake can improve the interface compatibility between the electrode and electrolyte. In contrast, massive electrolyte uptake also decreases the interaction capability between the binder and other electrode components by the softening and solvation of the binder.[40,41] Besides, an abundance of electrolyte solution in electrodes deteriorates the ionic and electric conductions caused by excess electrolyte penetration.[42] Therefore, the relatively small electrolyte uptake of the HCS and MC-HCS binders can ensure good affinity for the electrolyte and structural integrity of the electrode. To examine the effect of the hollow core–shell on lithium ion transport, AC impedance was performed by sandwiching the polymer film between two stainless-steel electrodes. Figure S5 shows its results. The bulk resistances were obtained from the spike-like lines on the real axis in the Nyquist plot using the equivalent circuit inserted in the figure.[43−46] As presented in Figure 3c, the ionic conductivities of the HCS and MC-HCS calculated from the bulk resistances are 44.3 and 55.8 μS cm^{-1} at room temperature, respectively, which are much larger than that of the CS binder of 6.9 μS cm^{-1} and the SBR binder of 5.9 μS cm^{-1}. This indicates that the hollow core is an efficient binder structure facilitating lithium ion transport compared with the compact core structure of the CS binder. It is consistent to the result reported by Chen et al.[47] that the hollow structures with a thin shell facilitate the transport of ions.

Before the hollow core–shell samples were finally applied in the binder for Si anodes, their thermal stabilities were investigated through TGA because the materials are exposed to high temperatures during electrode drying. Figure S6 shows the experimental results of an exhibit that the HCS and MC-HCS binder films begin to decompose at approximately 340 °C. Although their decomposition occurs earlier than that of the CS polymer film of 380 °C, the decomposition temperatures of the HCS and MC-HCS are high enough compared to the electrode drying temperature, so they are thermally stable as the binder for the Si electrodes.

The intrinsic hurdle of the high-capacity Si anodes is that the volumetric expansion and contraction of the Si particles reach 310% during lithium ion insertion and desertion, leading to the electrical isolation of the electrode. Therefore, the adhesion ability and resistance of Si electrodes are key factors determining the electrochemical behavior of the high-capacity anode during cell operation. Figure 3d shows the results of the adhesion ability of electrodes with different binders to examinations. The average adhesion strengths of the electrodes fabricated by the SBR and CS binders are lower than 0.5 N, whereas the Si electrodes composed of the HCS and MC-HCS binders show higher adhesive strengths of 0.952 and 0.692 N, respectively. As shown in Figure 1 and mentioned, the core polymer coming out and being dissolved into a binder solution during the alkalization treatment possesses highly adhesive carboxy anion (COO^-) functional groups. This could improve the adhesion strength of

https://doi.org/10.1021/acsomega.3c07752
ACS Omega 2023, 8, 49302−49310

the Si electrode. However, the decrease in the adhesion of the MXene-containing HCS is inevitable due to the increase in the electrode surface's ability to adhere.

On the other hand, the Si electrodes' electrical interface resistance and volumetric resistivity are improved by the MXene in the binder, as exhibited in Figure 3e. The volume resistivity and interface resistance of the Si electrode containing the MC-HCS binder are 3.97×10^{-2} Ω cm and 4.93×10^{-5} Ω cm^2, respectively, which are the lowest among those containing the other binders, including the conventional SBR binder. This illustrates that introducing a conductive MXene to a water-based binder can improve the electrode conductivity and adhesion by the empty-core structure compared with the conventional core−shell SBR binder.

The electrochemical performances of the Si anodes were examined using CR2032-type coin half-cells at room temperature. As displayed in Figure S7, all CV curves of the Si electrodes show similar electrochemical behaviors. Wide cathodic peaks in the first cycle are observed in the voltage range of 0.5−1.5 V, which are attributed to electrolyte decomposition and the SEI layer formation.[48−50] However, the peaks disappear in the following cycles, explaining that the SEI layer on the surface of active materials has been completed at the first cathodic sweep. The sharp anodic peaks around 0.58 V are associated with the delithiation of amorphous Li_xSi, and clear cathodic peaks are also present around 0 V, corresponding to the lithiation of Si. To compare the electrochemical activity in the different binders of the Si electrodes, the third CV profiles of the silicon electrodes containing different binders are selected and are redrawn in Figure 4a. Despite the improvement in the ionic conductivity by the hollow core−shell structure, there is no distinguishable change in the CV profiles between the CS- and HCS-containing electrodes. It must be caused by intrinsic low ionic conduction of polymeric binders, compared to the liquid electrolyte. However, the MC-HCS-containing Si electrode exhibits distinct redox peak intensities resulting from lithiation and delithiation of Si, whereas the other electrodes show sluggish CV profiles. In addition, the difference in the redox peak potentials is smaller than that of any other electrodes. Therefore, introducing MCs facilitates redox reactivity due to its high electronic conductivity.[51]

The electrochemical impedance of the 100-cycled cells operates at 0.2 V with an amplitude of 7 mV. The Nyquist plots shown in Figure 4b consist of three main regions: two compressed semicircles corresponding to the solid interfacial resistance (R_{sei}) in the high-frequency range and the charge transfer resistance (R_{ct}) in the middle-frequency range and a straight line in the low-frequency range belonging to the diffusion of lithium ions.[48] As shown in the inset in Figure 4b, the R_{sei} values of SBR-, CS-, HCS-, and MC-HCS-containing Si electrodes are 12.8, 7.9, 2.7, and 0.6 Ω, respectively. Compared to the CS electrode, the HCS and MC-HCS electrodes have much smaller R_{sei}, implying that MXenes in electrodes can keep an integrated electrical network and prevent the formation of a thick SEI layer on the surface of silicon particles. A thick SEI layer is unstable and cannot tolerate volumetric expansion during lithiation and delithiation.[52] The electrode fabricated with an HCS binder shows a lower charge transfer resistance of 21.8 Ω compared to that of SBR of 123 Ω and CS 50.3 Ω, attributed to the good ionic conductivity and high adhesive strength of the HCS in Figure 3c,d, respectively.[53,54] Furthermore, the R_{ct} value of 5.9 Ω of the MC-HCS electrode becomes smaller than that of the HCS electrode. Such a low charge transfer resistance must be influenced by high ionic conductivity and low resistance in Figure 3c,e.[14,55,56] In summary, the hollow core−shell structure is facile for ions to be transported in the Si electrode, and the existence of MC is helpful in constructing the electrical network of the Si electrodes.

Figure 4c,d shows the cycling performance and rate capability of Si-based electrodes with different binders. All electrodes were charged/discharged at 0.1C for the first two cycles and 0.5C for the subsequent 100 cycles. Stable coulombic efficiency is an essential parameter for long cycling performance.[57] The electrodes with the MC-HCS binder display ascending coulombic efficiency (more than 95% since the third cycle and keep around 98% after 50 cycles), while others show low ascending coulombic efficiency (lower than 90% at the third cycle and lower than 95% after the cycles). As a result, the MC-HCS electrode shows a superior capacity retention of 1351 mAg^{-1} at 0.5C after 100 cycles. In contrast, the HCS electrode is 713 mAh g^{-1}, and the CS and SBR electrodes are only 203 mAh g^{-1} left. The electrodes without MC exhibit rapid capacity fading during 100 cycles, often detected when cracks in the high-capacity electrode lead to electrical isolation. On the other hand, the MC-HCS electrode shows a more stable cycling capacity, indicating that the conductive MC in the binder maintains electrical networks even in the cracked electrode. These phenomena were observed in the rate capability test shown in Figure 4d. The MC-HCS electrode provides a better rate capability than that of others. The capacity drop of the MC-HCS is much smaller than that of the others, even at a high current density of 5C, and the electrode maintains a capacity retention of 1100 mAh g^{-1}. On the contrary, the capacities of HCS, CS, and SBR electrodes decrease rapidly as the current density increases. Also, at 5C, it dramatically drops to 750 mAh g^{-1} for the HCS and less than 250 mAh g^{-1} for the CS and SBR. The Si electrode containing the MC-HCS binder recovers its potential very well when the current drops to 0.1C. It should be noticed that the contribution of the MC to the capacity is negligible because its amount is 0.167 wt % in the electrode and the theoretical capacity of bare MCs is relatively small (320 mAh g^{-1}).[58]

Different amounts of MCs were physically mixed with the HCS binder during the slurry preparation process to further investigate the effects of the in situ polymerized binder on MCs. Regardless of the physically mixed MC amount, the binder content, including MCs, remains 10 wt % in electrodes. Thus, the HCS/MC-0.5, -1, and -2% samples contain HCS and MCs of 9.5:0.5%, 9:1%, and 8:2% in the electrodes, respectively. The electrochemical performances are exhibited in Figure 4e,f. As expected, the increase in the amount of physically mixed MCs decreases the impedance of the Si electrode, as shown in Figure 4e. However, their R_{sei} and R_{ct} are much larger than those of the Si electrode fabricated by the in-site polymerized MC-HCS binder (Figure 4b). Moreover, the cycling performance test results are much worse regardless of the amount of the physically mixed MCs compared to the MC-HCS-containing Si electrode, as shown in Figure 4f. These indicate that the physically mixed MC could not prevent the loss of reversible storage sites due to the electrical isolation.[59] As seen in Figure S8, MCs are not homogenously dispersed in the HCS binder solution and are rather sedimented. On the contrary, the in situ polymerized MC-HCS binder is well dispersed and looks stable in the solution, as shown in Figure S1. Above all, the homogenous dispersion of the MC-HCS binder could maintain the electrical network even

https://doi.org/10.1021/acsomega.3c07752
ACS Omega 2023, 8, 49302−49310

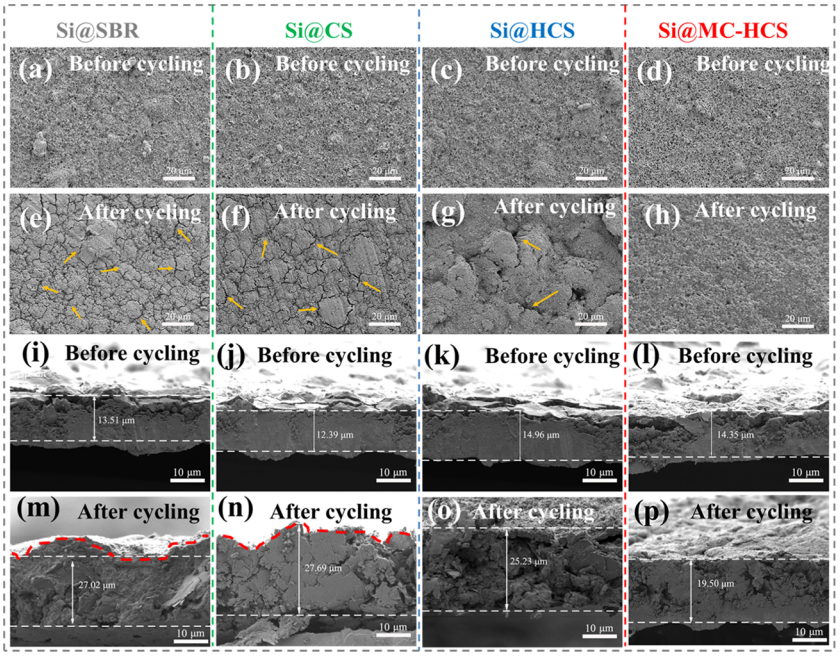

Figure 5. Top-view SEM images of the Si electrodes with (a) SBR, (b) CS, (c) HCS, and (d) MC-HCS before cycling and (e) SBR, (f) CS, (g) HCS, and (h) MC-HCS after 50 cycles. The cross-sectional images of the Si electrodes with (i) SBR, (j) CS, (k) HCS, and (l) MC-HCS before cycling and (m) SBR, (n) CS, (o) HCS, and (p) MC-HCS after 50 cycles.

during the charge/discharge process of Si accompanying huge volume change.

SEM images and digital photographs were taken to better investigate the morphological evolution during cycling. According to the top-viewed SEM images shown in Figure 5a–h, all electrodes with different binders exhibit unbroken and smooth surfaces before the charge/discharge cycle. However, after 50 cycles, the electrodes with the SBR, CS and HCS show serious cracks. In contrast, the electrodes fabricated using the MC-HCS binder maintain the structure integral and crack-free morphology. The volume expansion rate of electrodes was calculated from cross-sectional SEM analysis shown in Figure 5i–p. The thickness changes of Si electrodes containing the SBR, CS, HCS, and MC-HCS are 13.51, 15.30, 10.27, and 5.15 μm, respectively. Thus, the MC-HCS electrodes demonstrate the lowest volume expansion rate of 36% compared with the electrodes of SBR (100%), CS (124%), and HCS (68%) electrodes. Such phenomena indicate that the MC-HCS binder could enable silicon surface stability by providing a complete electrical network and alleviating thick SEI layer formation, together with avoiding silicon particle breaking and structure collapse. This is also confirmed from the digital photos shown in Figure S9. The electrodes composed of SBR, CS, and HCS binders experience partial delamination around their edges after cycling, whereas the MC-HCS containing the electrode maintains its original shape without electrode delamination.

4. CONCLUSIONS

We have successfully developed an MXene clay/water-based acrylate composite binder for the silicon anode. The addition of MXene clay alleviates the electrical isolation of silicon electrodes after the huge volumetric change, and the hollow core–shell structure of the polymer could improve the ionic conductivity. Moreover, the in situ polymerized MC-HCS binder makes the MXene clay and acrylate binder connect strongly and homogenously rather than providing a weak connection through physical blending. These ensure that the MC-HCS binder is appropriate for electrolyte affinity and better ionic conductivity and guarantees excellent electrochemical performance in a high-capacity silicon anode. The high capacity retention, 1351 mAh g^{-1} after 100 cycles at 0.5C, of silicon electrodes containing the MC-HCS binder is approximately 2 times greater than that containing the HCS with no MCs, which is much larger than those containing the CS with no MCs and no hollow core as well as the commercial SBR binder. The in situ acrylate polymerization with MCs is much more favorable to the electrochemical performance of the binder when compared to the physical mixing of MCs with the acrylate binder. The novel strategy of combining a conductive MXene and adhesive water-dispersed acrylate binder by in situ emulsion polymerization provides a new way to design and synthesize an ecofriendly water-based binder for high-capacity silicon anodes.

■ ASSOCIATED CONTENT

Supporting Information

The Supporting Information is available free of charge at https://pubs.acs.org/doi/10.1021/acsomega.3c07752.

Recipe for the synthesis of CS, HCS, and MC-HCS binders, photographs of the sonicated MXene clay solution and polymerized MC-HCS binder latex, differential scanning calorimetry thermograms of the CS polymer solid film, FT-IR and Raman spectroscopy of CS, HCS, and MC-HCS binders, dynamic viscosity of CS, HCS, and MC-HCS latex, Nyquist plot of the polymer film sandwiched by two stainless-steel electrodes, thermogravimetry (TGA) of CS, HCS, and MC-HCS polymer films, CV profiles of the silicon electrodes containing different binders: SBR, CS, HCS, and MC-HCS electrodes, photographs of the HCS binder and physically mixed HCS/MC, and digital photographs of the electrodes with different binders before and after cycling (PDF)

https://doi.org/10.1021/acsomega.3c07752
ACS Omega 2023, 8, 49302–49310

AUTHOR INFORMATION

Corresponding Authors

Wenjun Gan − *Department of Macromolecular Materials and Engineering, College of Chemistry and Chemical Engineering, Shanghai University of Engineering Science, 201620 Shanghai, China;* orcid.org/0000-0002-3671-5900; Email: wjgan@sues.edu.cn

Eun-Suok Oh − *School of Chemical Engineering, University of Ulsan, Ulsan 44610, Republic of Korea;* orcid.org/0000-0003-1954-5361; Phone: (82)-52-259-2783; Email: esoh1@ulsan.ac.kr; Fax: (82)-52-259-1689

Author

Mi Tian − *School of Chemical Engineering, University of Ulsan, Ulsan 44610, Republic of Korea; Department of Macromolecular Materials and Engineering, College of Chemistry and Chemical Engineering, Shanghai University of Engineering Science, 201620 Shanghai, China*

Complete contact information is available at: https://pubs.acs.org/10.1021/acsomega.3c07752

Notes

The authors declare no competing financial interest.

ACKNOWLEDGMENTS

The work was supported by the National Research Foundation of Korea grants funded by the Ministry of Science ICT(MSIT) [NRF-2022R1A2C101306812, 2021RIS-003] and by the Industrial Strategic Technology Development Program [20009866] and the Korea Institute for Advancement of Technology grant [P0023727] funded by the Ministry of Trade, Industry and Energy (MOTIE, Korea).

REFERENCES

(1) Son, I. H.; Hwan Park, J.; Kwon, S.; Park, S.; Rümmeli, M. H.; Bachmatiuk, A.; Song, H. J.; Ku, J.; Choi, J. W.; Choi, J.; Doo, S.-G.; Chang, H. Silicon carbide-free graphene growth on silicon for lithium-ion battery with high volumetric energy density. *Nat. Commun.* **2015**, *6*, No. 7393.

(2) Wu, H.; Cui, Y. Designing nanostructured Si anodes for high energy lithium ion batteries. *Nano Today* **2012**, *7*, 414−429.

(3) Li, X.; Gu, M.; Hu, S.; Kennard, R.; Yan, P.; Chen, X.; Wang, C.; Sailor, M. J.; Zhang, J.-G.; Liu, J. Mesoporous silicon sponge as an anti-pulverization structure for high-performance lithium-ion battery anodes. *Nat. Commun.* **2014**, *5*, No. 4105.

(4) Qi, C.; Li, S.; Yang, Z.; Xiao, Z.; Zhao, L.; Yang, F.; Ning, G.; Ma, X.; Wang, C.; Xu, J.; Gao, J. Suitable thickness of carbon coating layers for silicon anode. *Carbon* **2022**, *186*, 530−538.

(5) Sun, L.; Liu, Y.; Shao, R.; Wu, J.; Jiang, R.; Jin, Z. Recent progress and future perspective on practical silicon anode-based lithium ion batteries. *Energy Storage Mater.* **2022**, *46*, 482−502.

(6) Sun, L.; Jiang, X.; Jin, Z. Interfacial engineering of porous SiOx@C composite anodes toward high-performance lithium-ion batteries. *Chem. Eng. J.* **2023**, *474*, No. 145960.

(7) Huang, Q.; Song, J.; Gao, Y.; Wang, D.; Liu, S.; Peng, S.; Usher, C.; Goliaszewski, A.; Wang, D. Supremely elastic gel polymer electrolyte enables a reliable electrode structure for silicon-based anodes. *Nat. Commun.* **2019**, *10*, No. 5586.

(8) Chen, J.; Naveed, A.; NuLi, Y.; Yang, J.; Wang, J. Designing an intrinsically safe organic electrolyte for rechargeable batteries. *Energy Storage Mater.* **2020**, *31*, 382−400.

(9) Chen, J.; Fan, X.; Li, Q.; Yang, H.; Khoshi, M. R.; Xu, Y.; Hwang, S.; Chen, L.; Ji, X.; Yang, C.; He, H.; Wang, C.; Garfunkel, E.; Su, D.; Borodin, O.; Wang, C. Electrolyte design for LiF-rich solid−electrolyte interfaces to enable high-performance microsized alloy anodes for batteries. *Nat. Energy* **2020**, *5*, 386−397.

(10) Shi, Z.; Liu, Q.; Yang, Z.; Robertson, L. A.; Bheemireddy, S. R.; Zhao, Y.; Zhang, Z.; Zhang, L. A chemical switch enabled autonomous two-stage crosslinking polymeric binder for high performance silicon anodes. *J. Mater. Chem. A* **2022**, *10*, 1380−1389.

(11) Niu, S.; Zhao, M.; Ma, L.; Zhao, F.; Zhang, Y.; Tang, G.; Wang, Y.; Pang, A.; Li, W.; Wei, L. High performance polyurethane−polyacrylic acid polymer binders for silicon microparticle anodes in lithium-ion batteries. *Sustainable Energy Fuels* **2022**, *6*, 1301.

(12) Wang, Y.; Xu, H.; Chen, X.; et al. Novel constructive self-healing binder for silicon anodes with high mass loading in lithium-ion batteries. *Energy Storage Mater.* **2021**, *38*, 121−129.

(13) Kwon, T.-w.; Choi, J. W.; Coskun, A. The emerging era of supramolecular polymeric binders in silicon anodes. *Chem. Soc. Rev.* **2018**, *47*, 2145−2164.

(14) Nam, J.; Kim, E.; K, R. K.; Kim, Y.; Kim, T.-H. A conductive self healing polymeric binder using hydrogen bonding for Si anodes in lithium ion batteries. *Sci. Rep.* **2020**, *10*, No. 14966.

(15) Zhao, Y.-M.; Yue, F.-S.; Li, S.-C.; Zhang, Y.; Tian, Z.-R.; Xu, Q.; Xin, S.; Guo, Y.-G. Advances of polymer binders for silicon-based anodes in high energy density lithium-ion batteries. *InfoMat.* **2021**, *3*, 460−501.

(16) Yu, Y.; Zhu, J.; Zeng, K.; Jiang, M. Mechanically robust and superior conductive n-type polymer binders for high-performance micro-silicon anodes in lithium-ion batteries. *J. Mater. Chem. A* **2021**, *9*, 3472−3481.

(17) Cao, S.; Shen, B.; Tong, T.; Fu, J.; Yu, J. 2D/2D Heterojunction of Ultrathin MXene/Bi2WO6 Nanosheets for Improved Photocatalytic CO2 Reduction. *Adv. Funct. Mater.* **2018**, *28*, No. 1800136.

(18) Zhang, J.; Zhao, Y.; Guo, X.; Chen, C.; Dong, C.-L.; Liu, R.-S.; Han, C.-P.; Li, Y.; Gogotsi, Y.; Wang, G. Single platinum atoms immobilized on an MXene as an efficient catalyst for the hydrogen evolution reaction. *Nat. Catal.* **2018**, *1*, 985−992.

(19) Song, S.; Zhang, C.; Li, W.; Wang, J.; Rao, P.; Wang, J.; Li, T.; Zhang, Y. Bioinspired engineering of gradient and hierarchical architecture into pressure sensors toward high sensitivity within ultra-broad working range. *Nano Energy* **2022**, *100*, No. 107513.

(20) Wu, X.; Liao, H.; Ma, D.; Chao, M.; Wang, Y.; Jia, X.; Wan, P.; Zhang, L. A wearable, self-adhesive, long-lastingly moist and healable epidermal sensor assembled from conductive MXene nanocomposites. *J. Mater. Chem. C* **2020**, *8*, 1788−1795.

(21) Pang, J.; Mendes, R. G.; Bachmatiuk, A.; Zhao, L.; Ta, H. Q.; Gemming, T.; Liu, H.; Liu, Z.; Rummeli, M. H. Applications of 2D MXenes in energy conversion and storage systems. *Chem. Soc. Rev.* **2019**, *48*, 72−133.

(22) Yang, Q.; Wang, Y.; Li, X.; Li, H.; Wang, Z.; Tang, Z.; Ma, L.; Mo, F.; Zhi, C. Recent Progress of MXene-Based Nanomaterials in Flexible Energy Storage and Electronic Devices. *Energy Environ. Mater.* **2018**, *1*, 183−195.

(23) Naguib, M.; Kurtoglu, M.; Presser, V.; Lu, J.; Niu, J.; Heon, M.; Hultman, L.; Gogotsi, Y.; Barsoum, M. W. Two-Dimensional Nanocrystals Produced by Exfoliation of Ti3AlC2. *Adv. Mater.* **2011**, *23*, 4248−4253.

(24) Naguib, M.; Mashtalir, O.; Carle, J.; Presser, V.; Lu, J.; Hultman, L.; Gogotsi, Y.; Barsoum, M. W. Two-Dimensional Transition Metal Carbides. *ACS Nano* **2012**, *6*, 1322.

(25) Ronchi, R. M.; Arantes, J. T.; Santos, S. F. Synthesis, structure, properties and applications of MXenes: Current status and perspectives. *Ceram. Int.* **2019**, *45*, 18167−18188.

(26) Pan, Q.; Zheng, Y.; Kota, S.; Huang, W.; Wang, S.; Qi, H.; Kim, S.; Tu, Y.; Barsoum, M. W.; Li, C. Y. 2D MXene-containing polymer electrolytes for all-solid-state lithium metal batteries. *Nanoscale Adv.* **2019**, *1*, 395−402.

(27) Xu, H.; Yin, X.; Li, X.; Li, M.; Liang, S.; Zhang, L.; Cheng, L. Lightweight Ti2CTx MXene/Poly(vinyl alcohol) Composite Foams for Electromagnetic Wave Shielding with Absorption-Dominated Feature. *ACS Appl. Mater. Interfaces* **2019**, *11*, 10198.

(28) Huang, X.; Wang, R.; Jiao, T.; Zou, G.; Zhan, F.; Yin, J.; Zhang, L.; Zhou, J.; Peng, Q. Facile Preparation of Hierarchical AgNP-Loaded MXene/Fe3O4/Polymer Nanocomposites by Electrospinning with Enhanced Catalytic Performance for Wastewater Treatment. *ACS Omega* **2019**, *4*, 1897.
(29) Tu, S.; Jiang, Q.; Zhang, X.; Alshareef, H. N. Large Dielectric Constant Enhancement in MXene Percolative Polymer Composites. *ACS Nano* **2018**, *12*, 3369.
(30) Ling, Z.; Ren, C. E.; Zhao, M.-Q.; Yang, J.; Giammarco, J. M.; Qiu, J.; Barsoum, M. W.; Gogotsi, Y. Flexible and conductive MXene films and nanocomposites with high capacitance. *Proc. Natl. Acad. Sci. U.S.A.* **2014**, *111*, 16676−16681.
(31) Sun, R.; Zhang, H.-B.; Liu, J.; Xie, X.; Yang, R.; Li, Y.; Hong, S.; Yu, Z.-Z. Highly Conductive Transition Metal Carbide/Carbonitride-(MXene)@polystyrene Nanocomposites Fabricated by Electrostatic Assembly for Highly Efficient Electromagnetic Interference Shielding. *Adv. Funct. Mater.* **2017**, *27*, No. 1702807.
(32) Yang, J.; Bao, W.; Jaumaux, P.; Zhang, S.; Wang, C.; Wang, G. MXene-Based Composites: Synthesis and Applications in Rechargeable Batteries and Supercapacitors. *Adv. Mater. Interfaces* **2019**, *6*, No. 1802004.
(33) Liao, Y.; Li, W.; Rao, M. M.; et al. Fumed silica-doped poly(butyl methacrylate-styrene)-based gel polymer electrolyte for lithium ion battery. *J. Membr. Sci.* **2010**, *352*, 95−99.
(34) Lee, J. T.; Chu, Y.; Peng, X.; Li, C.; et al. A novel and efficient water-based composite binder for LiCoO2 cathodes in lithium-ion batteries. *J. Power Sources* **2007**, *173*, 985−989.
(35) Yuan, C.-D.; Miao, A.-H.; Cao, J.-W.; Xu, Y.-S.; Cao, T.-Y. Preparation of monodispersed hollow polymer particles by seeded emulsion polymerization under low emulsifier conditions. *J. Appl. Polym. Sci.* **2005**, *98*, 1505−1510.
(36) Huang, Y.; Huang, Y.; Liu, B.; Cao, H.; Zhao, L.; et al. Gel polymer electrolyte based on p(acrylonitrile-maleic anhydride) for lithium ion battery. *Electrochim. Acta* **2018**, *286*, 242−251.
(37) Liao, Y.; Zhou, D.; Rao, M. M.; Li, W.; Cai, Z.; et al. Self-supported poly(methyl methacrylate−acrylonitrile−vinyl acetate)-based gel electrolyte for lithium ion battery. *J. Power Sources* **2009**, *189*, 139−144.
(38) Gao, Y.; Qiu, X.; Wang, X.; Gu, A.; Zhang, L.; Chen, X.; Li, J.; Yu, Z. Chitosan-g-Poly(acrylic acid) Copolymer and Its Sodium Salt as Stabilized Aqueous Binders for Silicon Anodes in Lithium-Ion Batteries. *ACS Sustainable Chem. Eng.* **2019**, *7*, 16274.
(39) Jang, S.-Y.; Han, S.-H. Fabrication of Si negative electrodes for Li-ion batteries (LIBs) using cross-linked polymer binders. *Sci. Rep.* **2016**, *6*, No. 38050.
(40) Zhao, L.; Sun, Z.; Zhang, H.; Li, Y.; Mo, Y.; Yu, F.; Chen, Y. An environment-friendly crosslinked binder endowing LiFePO 4 electrode with structural integrity and long cycle life performance. *RSC Adv.* **2020**, *10*, 29362−29372.
(41) Lee, S.-Y.; Choi, Y. C.; Kwon, S.-H.; Bae, J.-S.; Jeong, E. D. Cracking resistance and electrochemical performance of silicon anode on binders with different mechanical characteristics. *J. Ind. Eng. Chem.* **2019**, *74*, 216−222.
(42) Komaba, S.; Shimomura, K.; Yabuuchi, N.; Ozeki, T.; Yui, H.; Konno, K. Study on Polymer Binders for High-Capacity SiO Negative Electrode of Li-Ion Batteries. *J. Phys. Chem. C* **2011**, *115*, 13487.
(43) Zhang, J.; Sun, B.; Huang, X.; Chen, S.; Wang, G. Honeycomb-like porous gel polymer electrolyte membrane for lithium ion batteries with enhanced safety. *Sci. Rep.* **2014**, *4*, No. 6007.
(44) Brza, M.; Aziz, S. B.; Raza Saeed, S.; Hamsan, M. H.; Majid, S. R.; Abdulwahid, R. T.; Kadir, M.F.Z.; Abdullah, R. M. Energy Storage Behavior of Lithium-Ion Conducting poly(vinyl alcohol) (PVA): Chitosan(CS)-Based Polymer Blend Electrolyte Membranes: Preparation, Equivalent Circuit Modeling, Ion Transport Parameters, and Dielectric Properties. *Membranes* **2020**, *10*, No. 381, DOI: 10.3390/membranes10120381.
(45) Bérardan, D.; Franger, S.; Meena, A. K.; Dragoe, N. Room temperature lithium superionic conductivity in high entropy oxides. *J. Mater. Chem. A* **2016**, *4*, 9536−9541.
(46) Kamaya, N.; Homma, K.; Yamakawa, Y.; Hirayama, M.; Kanno, R.; Yonemura, M.; Kamiyama, T.; Kato, Y.; Hama, S.; Kawamoto, K.; Mitsui, A. A lithium superionic conductor. *Nat. Mater.* **2011**, *10*, 682−686.
(47) Chen, Z.; Zhao, M.; Lv, X.; Zhou, K.; Jiang, X.; Ren, X.; Mei, X. Fast ion transport through ultrathin shells of metal sulfide hollow nanocolloids used for high-performance energy storage. *Sci. Rep.* **2018**, *8*, No. 30.
(48) Luo, C.; Du, L.; Wu, W.; Xu, H.; Zhang, G.; Li, S.; Wang, C.; Lu, Z.; Deng, Y. Novel Lignin-Derived Water-Soluble Binder for Micro Silicon Anode in Lithium-Ion Batteries. *ACS Sustainable Chem. Eng.* **2018**, *6*, 12621.
(49) Xie, Z. H.; Rong, M. Z.; Zhang, M. Q. Dynamically Cross-Linked Polymeric Binder-Made Durable Silicon Anode of a Wide Operating Temperature Li-Ion Battery. *ACS Appl. Mater. Interfaces* **2021**, *13*, 28737−28748.
(50) Wang, Z.; Huang, T.; Yu, A. A carboxymethyl vegetable gum as a robust water soluble binder for silicon anodes in lithium-ion batteries. *J. Power Sources* **2021**, *489*, No. 229530.
(51) Gund, G. S.; Park, J.; Park, H.; Gogotsi, Y.; et al. MXene/Polymer Hybrid Materials for Flexible AC-Filtering Electrochemical Capacitors. *Joule* **2019**, *3*, 164−176.
(52) Han, L.; Liu, T.; Sheng, O.; Liu, Y.; Wang, Y.; Nai, J.; Zhang, L.; Tao, X. Undervalued Roles of Binder in Modulating Solid Electrolyte Interphase Formation of Silicon-Based Anode Materials. *ACS Appl. Mater. Interfaces* **2021**, *13*, 45139.
(53) Munaoka, T.; Yan, X.; Lopez, J.; To, J. W. F.; Park, J.; Tok, J.B.-H.; Cui, Y.; Bao, Z. Ionically Conductive Self-Healing Binder for Low Cost Si Microparticles Anodes in Li-Ion Batteries. *Adv. Energy Mater.* **2018**, *8*, No. 1703138.
(54) Hu, S.; Wang, L.; Huang, T.; Yu, A. A conductive self-healing hydrogel binder for high-performance silicon anodes in lithium-ion batteries. *J. Power Sources* **2020**, *449*, No. 227472.
(55) Zheng, M.; Wang, C.; Xu, Y.; Li, K.; Liu, D. A water-soluble binary conductive binder for Si anode lithium ion battery. *Electrochim. Acta* **2019**, *305*, 555−562.
(56) Zhao, Y.; Yang, L.; Zuo, Y.; Song, Z.; Liu, F.; Li, K.; Pan, F. Conductive Binder for Si Anode with Boosted Charge Transfer Capability via n-Type Doping. *ACS Appl. Mater. Interfaces* **2018**, *10*, 27795.
(57) Sun, L.; Liu, Y.; Wu, J.; Shao, R.; Jiang, R.; Tie, Z.; Jin, Z. A Review on Recent Advances for Boosting Initial Coulombic Efficiency of Silicon Anodic Lithium Ion batteries. *Small* **2022**, *18*, No. 2102894.
(58) Xie, Y.; Naguib, M.; Mochalin, V. N.; Barsoum, M. W.; Gogotsi, Y.; Yu, X.; Nam, K.-W.; Yang, X.-Q.; Kolesnikov, A. I.; Kent, P. R. C. Role of Surface Structure on Li-Ion Energy Storage Capacity of Two-Dimensional Transition-Metal Carbides. *J. Am. Chem. Soc.* **2014**, *136*, 6385−6394.
(59) Song, J.; Zhou, M.; Yi, R.; Xu, T.; Gordin, M. L.; Tang, D.; Yu, Z.; Regula, M.; Wang, D. Interpenetrated Gel Polymer Binder for High-Performance Silicon Anodes in Lithium-ion Batteries. *Adv. Funct. Mater.* **2014**, *24*, 5904−5910.

https://doi.org/10.1021/acsomega.3c07752
ACS Omega 2023, 8, 49302−49310